



Er³⁺ doped bismuth molybdate nanosheets with exposed {0 1 0} facets and enhanced photocatalytic performance

Tengfei Zhou, Juncheng Hu*, Jinlin Li

Key Laboratory of Catalysis and Materials Science of the State Ethnic Affairs Commission & Ministry of Education, Hubei Province, South-Central University for Nationalities, Wuhan 430074, PR China

ARTICLE INFO

Article history:

Received 6 May 2011

Received in revised form 27 August 2011

Accepted 7 September 2011

Available online 14 September 2011

Keywords:

Upconversion

Erbium

{0 1 0} facets

Bismuth molybdate

Photocatalysis

ABSTRACT

Er³⁺ doped Bi₂MoO₆ nanosheets with enhanced photocatalytic activity were synthesized for the first time using a simple hydrothermal method. The morphology of Bi₂MoO₆ can be controlled from nanosheets to nanowires by adjusting the pH values. The samples were characterized by transmission electron microscopy (TEM), X-ray diffraction (XRD), Brunauer–Emmett–Teller (BET), photoluminescence spectra (PL) and X-ray photoelectron spectroscopy (XPS). Er³⁺ doped Bi₂MoO₆ nanosheets selectively exposed {0 1 0} facets as the main external surfaces and the nanowires grew along the (0 1 0) direction. The nanosheets were found to be highly active for photocatalytic degradation of dyes and phenol. The activities of the Er³⁺ doped Bi₂MoO₆ nanosheets were much superior to that of commercial Degussa P25. The effect of Er³⁺ on the photocatalytic activity of Bi₂MoO₆ was investigated in detail. The enhanced photocatalytic activity of Bi₂MoO₆ nanosheets can be attributed to the exposed {0 1 0} facets and the dopant Er³⁺ which can transform visible light into ultraviolet light.

© 2011 Elsevier B.V. All rights reserved.

1. Introduction

Natural energy, such as sunlight, can be used for environment remediation. As a green technology, photocatalysis has been obtained increasing interest because it can be widely applied to many domains that offer an economic and ecologically safe option to solve energy and pollution problems [1]. Various semiconductor materials have been synthesized in the past few decades [2]. However, fast recombination rate and poor solar efficiency (maximum 5%) have hindered the practical applications of most of these photocatalysts [3]. Natural sunlight that reaches the surface of the Earth is composed of medium and long wavelength UV light [UVB (280–320 nm); UVA (320–400 nm)], visible light (400–700 nm), and longer wavelengths. Ultraviolet light occupies only about 4% of the sunlight spectrum, but visible light occupies 43% of the solar spectrum. Various approaches have been developed to extend the response of photocatalysts from ultraviolet light into the visible-light region. Such as doping metallic (Pt, Au and Ag) and nonmetallic (C, N and F) elements in conventional photocatalysts to decrease the band gap in order to accommodate visible light photon energy [4–10], and the use of low band gap semiconductors including CdS, WO₃, BiVO₄, Bi₂WO₆ and Bi₂₀TiO₃₂ [11–16]. According to the formula $E_g = h\nu$ (h is Planck constant and ν is light frequency), the

photopotential energy excited by visible light is lower than that excited by ultraviolet light. Therefore, it is desirable to seek novel materials with high efficiency for energy conversion that can convert visible-light or near-infrared (NIR) into ultraviolet light. An alternative way is the utilization of an upconverter (UC).

Upconversion (UC) technique can utilize near-infrared or visible light excitation rather than UV excitation. Lanthanide doped UC nanoparticles can convert low-energy radiation (NIR or visible light) to higher energy radiation (UV) via multiple absorption and energy transfer [17–20]. Among various UC nanomaterials, Er³⁺ is a better dopant for upconverting of visible-light or NIR to ultraviolet light than the nonlinear crystals [21].

Bi₂MoO₆ is an active member of the Aurivillius oxide family that has attracted considerable attention because of its dielectric, ion-conductive, luminescent and catalytic properties [22–24]. Recent research revealed that Bi₂MoO₆ could perform as an excellent photocatalyst for water splitting and degradation of organic compounds [25–27]. However, pure Bi₂MoO₆ presents major photo absorption properties in the UV light region, which only occupies a small fraction of the solar spectrum. Fortunately, upconversion involves absorption of sub-band gap photons into an intermediate state followed by absorption of a second photon into the conduction band edge; the excited state subsequently relaxes back to the valence band edge, emitting higher energy photons. In the photocatalysis, the emitted higher energy photons can be absorbed to produce more electrons, and then the electrons could degrade the organic compound completely. For example, Er³⁺/Yb³⁺ co-doped

* Corresponding author. Tel.: +86 27 67841302.

E-mail address: junchenghuhu@hotmail.com (J. Hu).

TiO₂ phosphors have been applied to dye-sensitized solar cells to obtain longer wavelength response [28]. Theoretical estimation shows about 5% increase of the energy conversion efficiency by adding a rear upconverter in solar-energy-conversion materials under sunlight illumination [29]. Recently, near infrared light responsive photocatalysts involving YF₃:Yb, Tm/TiO₂, NaYF₄:Yb, Tm/CdS, Er³⁺ doped Bi₂WO₆ have been reported [30–32], but visible light responsive upconverter doped bismuth molybdate has not been reported.

Herein, for the first time, we describe an efficient hydrothermal crystallization approach to synthesize NIR and visible light responsive Er³⁺ doped Bi₂MoO₆ photocatalyst. The products were controllably synthesized with tunable morphology. By increasing the pH value of the reactant, the thickness of the nanosheets increased, and then nanowires formed. In this paper, we obtained a satisfied photocatalyst by optimizing the pH value of the reactant and Er³⁺ content. After capturing NIR and long wavelength photons, Er³⁺ emits relatively strong visible-light and UV light which matches very well with the band gap of Bi₂MoO₆. The effect of Er³⁺ on the photocatalytic activity of Bi₂MoO₆ was investigated in detail. Er³⁺ doped Bi₂MoO₆ was found to be highly effective for photocatalytic degradation of dyes and phenol.

2. Experimental

2.1. Materials and reagents

Bismuth nitrate (Bi(NO₃)₃·5H₂O), ammonium molybdate ((NH₄)₆Mo₇O₂₄·4H₂O), ethanol, anhydrous acetic acid, ammonia, phenol, and rhodamine-B (RhB) were provided by Sinopharm Chemical Reagent Co., Ltd. (Shanghai, China). Erbium nitrate (Er(NO₃)₃·6H₂O) was purchased from Alfa Aesar. All chemicals were analytical grade reagents and were used as received without further purification. Degussa P25 (~80% anatase and ~20% rutile) was purchased from Degussa (China) Co., Ltd. Deionized and doubly distilled water was used in this work.

2.2. Sample preparation

In a typical synthesis procedure, Bi(NO₃)₃·5H₂O (5 mmol) and (NH₄)₆Mo₇O₂₄·4H₂O (0.36 mmol) were dissolved in 10 mL anhydrous acetic acid and 60 mL doubly distilled water under vigorous magnetic stirring at room temperature, respectively. After the Bi(NO₃)₃·5H₂O dissolved completely, these two solutions were mixed together, then amorphous white precipitate formed immediately. The different pH values of the solution (2, 5, 8, 10 and 12) were then adjusted using concentrated ammonia under stirring. Afterward, aqueous solution containing desired amounts of Er(NO₃)₃·6H₂O was added for the synthesis of Er³⁺ doped Bi₂MoO₆. After being vigorously stirred for 1 h, the resulting precursor suspension was transferred into a 100 mL Teflon-lined stainless steel autoclave, which was subsequently heated to 160 °C and maintained for 24 h. Subsequently, the autoclave was cooled to room temperature naturally. The obtained samples were filtered, washed with deionized water and ethanol for several times, and then dried at 60 °C in air for 12 h.

2.3. Characterization

The crystalline structure of the catalysts was characterized by powder X-ray diffraction (XRD) employing a scanning rate of 0.05°/s in a 2θ range from 10° to 80°, in a Bruker D8 Advance using monochromatized Cu Kα (λ = 1.54 Å) radiation. The morphologies and sizes of the samples were observed by transmission electron microscopy (TEM), which were taken on a Tecnai G20 (FEI Co., Holland) TEM operating at 200 kV. The samples were supported on

a carbon film coated on a 3 mm diameter fine-mesh copper grid. A suspension in ethanol was sonicated, and a drop was dripped on to the support film. The Brunauer–Emmett–Teller (BET) specific surface areas of the samples were evaluated on the basis of nitrogen adsorption isotherms using a Micromeritics ASAP 2020 gas adsorption apparatus (USA). X-ray photoelectron spectroscopy (XPS) was recorded on a VG Multilab 2000 (VG Inc.) photoelectron spectrometer using monochromatic Al Kα radiation under vacuum at 2 × 10^{−6} Pa. All of the binding energies were referenced to the C 1s peak at 284.8 eV of the surface adventitious carbon. The ultraviolet–visible diffuse reflectance spectra were measured using the diffuse reflectance method with a Shimadzu UV-2450 spectrophotometer using an integrating sphere accessory. BaSO₄ was used as a reflectance standard in ultraviolet–visible diffuse reflectance experiments. The photoluminescence (PL) spectra of the samples were recorded with a PE LS 55 spectrofluorophotometer.

2.4. Photocatalytic measurement

In the photocatalytic dye rhodamine-B (RhB) or phenol degradation experiment under atmosphere, aqueous RhB (50 mL, 1 × 10^{−5} M) or phenol (50 mL, 20 mg L^{−1}) and 1 g L^{−1} of photocatalyst were placed in a Pyrex glass cell, which was in a optical system for the degradation reaction using a 350 W Xe lamp as simulated sunlight (wavelength from 200 to 800 nm) or visible light (wavelength > 420 nm, use a cutoff filter of 420 nm), and a filter (to prevent infrared irradiation) as the light source. Before illumination, the suspensions were prepared under an ultrasonic water bath for 10 min and magnetically stirred in the dark for 45 min to establish adsorption/desorption equilibrium between the organics and the catalyst. At given irradiation time intervals, 4 mL aliquots were collected, centrifuged, and then filtered through a Millipore filter (pore size 0.45 μm) to remove the catalyst particulates. An air conditioner was installed in the system to maintain the temperature at 20 °C.

The concentration of the organic dyes was determined by monitoring the height of the maximum of the absorbance in ultraviolet–visible spectra by a UV–vis/NIR spectrophotometer (UV-2450, Shimadzu). Total organic carbon (TOC) in the solution after phenol and organic dyes removal was measured by Analyser Multi N/C 3100 (Analytic Jena, Germany). Phenol in the reaction solution was analyzed on a Dionex high performance liquid chromatography (HPLC) instrument equipped with a Ultimate 3000 HPLC pump, Ultimate 3000 Variable wavelength Detector, and a intersil ODS-3 120 C18 reverse column (4.6 mm × 250 mm, particle size 5 μm, 120 Å, Dionex Bonded Silica products). The mobile-phase was 70% methanol and 30% water with a flow rate of 1 mL min^{−1}. The reproducibility of the results was checked by repeating the results at least three times and was found to be within acceptable limits (±5%).

3. Results and discussion

3.1. Characterization of bismuth molybdates

The Bi₂MoO₆ and Er³⁺ doped Bi₂MoO₆ samples prepared by hydrothermal crystallization approach at different pH values (pH 2–12) were characterized by X-ray diffraction (XRD), and the typical diffraction patterns are shown in Figs. 1 and 2. As can be seen from the XRD patterns, the high crystallinity can be obtained at different pH values, no signal for any other phases about erbium or impurities can be detected in the Er³⁺ doped Bi₂MoO₆ samples. No other diffraction peaks can be observed demonstrating that Er³⁺ doping in the hydrothermal synthesis does not have an effect

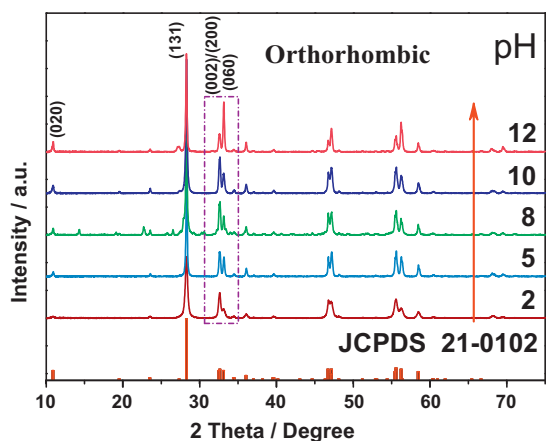


Fig. 1. XRD patterns of the as-prepared products at different pH values for 24 h at 160 °C.

on the crystalline phase of Bi₂MoO₆ due to the low content of Er³⁺. The diffraction peaks of all the samples can be indexed as a pure koechlinite phase, which are consistent with that of JCPDS 21-0102. The effect of pH value on the crystalline phase was demonstrated through the changes of XRD patterns. When the pH value is maintained at 5, the widened diffraction peaks obviously reveal that the crystalline phase would be nanosized. It is noteworthy that the XRD patterns also indicate that there are large differences in the relative intensities of the (020), (131), (200), (002) and (060) peaks for all the samples. For the samples prepared at acidic conditions (pH 2 and pH 5), the intensity ratio of (131)/(060) is about two, while the intensity of the (131) peak of the standard XRD pattern is about fivefold stronger than that of the (060) peak, indicating the possibility of different preferential orientation growths under different pH conditions. However, the changes of diffraction peaks of the samples obtained at basic conditions (pH 8–12) are different with the samples at acidic conditions (pH 2–5). The crystals grow along the (010) direction and form 1D wire-like materials. As the Er³⁺ content decreases from 2.0% to 0.5%, the intensities increase gradually, indicating that better crystallines formed.

The effects of pH values on the morphology of Er³⁺ doped Bi₂MoO₆ were studied by transmission electron microscopy (TEM). Fig. 3 shows the morphological evolution of Bi₂MoO₆ samples with different pH values (A–F: 2, 5, 8, 10 and 12). When the pH values in the reaction system are kept at 5, the thickness of sheet-like

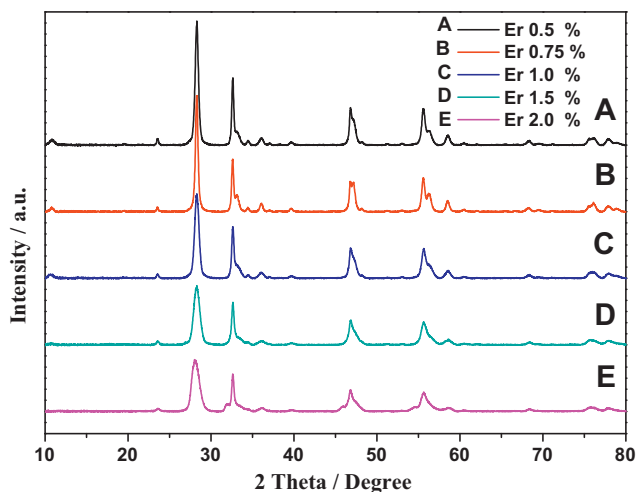


Fig. 2. XRD patterns of the as-prepared products with different Er³⁺ concentrations for 24 h at 160 °C.

Bi₂MoO₆ crystals are several nanometers (ca. 8 nm, Fig. 3B, pH 5). Interestingly, under acidic condition, the size of the Bi₂MoO₆ nanosheets becomes smaller with the increasing of the pH values. The width of the nanosheets is about 400 and 100 nm for samples A and B, respectively. Further increasing the pH value leads to the shape of the Bi₂MoO₆ nanostructures evolved from nanosheets to nanoplates with the thickness of tens of nanometers (ca. 30 nm, Fig. 3E, pH 10). The pH-dependent experiments are taken subsequently by increasing the pH values to 10 and 12. Fig. 2F exhibits some nanowires with an average diameter of about 20 nm and length of about 1 μm, which is very different from the morphologies of samples obtained under acidic conditions. The results suggest that the morphology of Bi₂MoO₆ nanosheets/microwires strongly depends on the initial pH values. Similar results were also observed in the synthesis of some tungstates [33]. Therefore, the morphology of the molybdate nanosheets/microwires can be controlled by tuning the pH values.

The nanoplate structure is clearly observed from Fig. 3D, which is in accordance with the TEM images. For the sample prepared at pH 8 and molar ratio for 1.0% Er³⁺ doped Bi₂MoO₆, the intensified (060) and (020) diffraction peaks compared with the characteristic (131) diffraction peak of Bi₂MoO₆ reveals that there is a preferred orientation of {010} plane. This phenomenon is also consistent with the HRTEM observation. For example, the HRTEM image of an individual sheet as shown in Fig. 4A indicates their single-crystalline nature and the calculated *d*-spacing of 2.75 and 2.74 Å correspond to the data of *d*(200) = 2.750 Å and *d*(002) = 2.741 Å, respectively. All the above characterizations show that the Bi₂MoO₆ sheets with a preferred [010] orientation and the surface can be indexed as {010} facet. One of the critical factors for the shape determination is the crystallographic phase of the initial seed. Once the crystalline phase is determined, the characteristic cell structures of the seeds strongly affect the crystal growth [34]. As it is shown in Fig. 4B, the structure of koechlinite Bi₂MoO₆ consists of alternating (Bi₂O₂)_n²⁺ layers and perovskite-like (MoO₄)_n²⁻ layers, and octahedral Mo chains usually play an important role in the high intrinsic anisotropic growth in various molybdates [35,36]. A possible formation process is schematically illustrated in Fig. 4C, in addition, with the transformation of Bi₂MoO₆ from a 2D sheet-like structure to a 1D wire-like nanostructure, the XRD pattern of the corresponding samples, the reflection intensity of (020), which is quite different from the standard data. The crystal plane with a higher surface energy is expected to have a faster growth rate. The formation process can be described as follows: at pH 2 and pH 5, there would be much more H⁺ in the system to be adsorbed on the (010) facets. Therefore, the surface energy of these facets would be markedly reduced. Thus, it is possible to form a relatively thin nature along [010] direction [37]. It is well known that the shape of the nanostructures is strongly dependent on the relative chemical potential and it is believed that two-dimensional growth occurs only if the chemical potential of two surfaces is much higher than others. Because the Bi₂MoO₆ has an orthorhombic crystal structure, crystal symmetries along *a* and *c* axes should be equivalent. From the experimental results, it can be concluded that under acidic condition, higher surface energy existed on the (200) and (002) planes compared with other crystal planes, and the growth of nanocrystal along the (010) plane was inhibited. However, when NH₃·H₂O was added to the solution, the acid was partially neutralized, which makes the concentration of H⁺ varied on the nanocrystal surface and results in the surface free energies of the various crystallographic planes differing significantly. Obviously, the growth rate of those facets possessing higher free energy would be relatively faster, which affords the possibility of breaking the natural growth habit of the crystal and creating additional growth anisotropy, therefore Bi₂MoO₆ nanowires can be obtained by tuning the pH of the growth solution. Under the

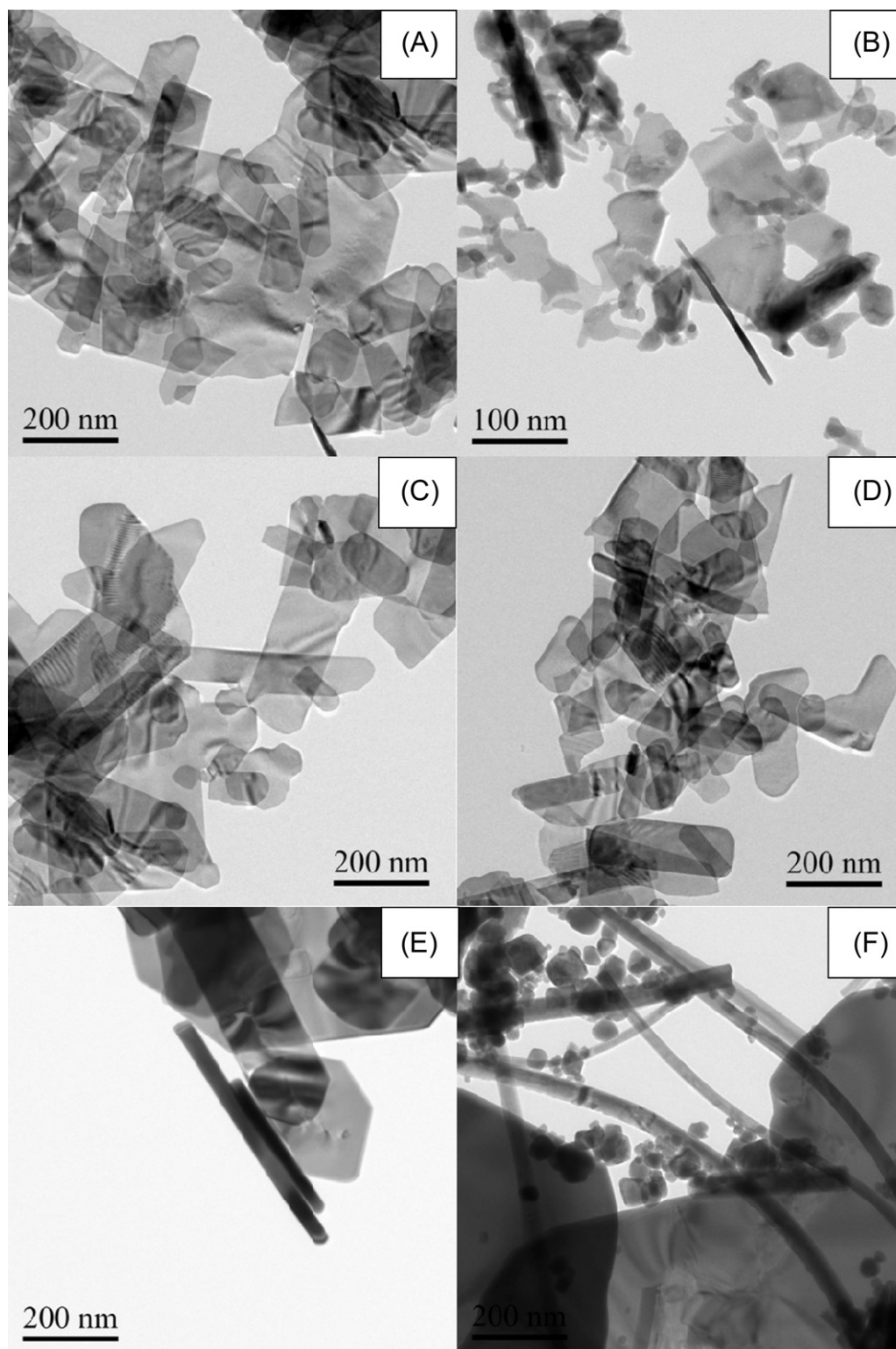


Fig. 3. TEM images of Bi_2MoO_6 samples prepared at different pH values. (A) pH 2, (B) pH 5, (C) pH 8, (D) pH 8 1.0% Er^{3+} -doped Bi_2MoO_6 , (E) pH 10, and (F) pH 12.

alkaline condition (pH 10 and 12), the dominant adsorption of OH^- onto the facets lowers the surface energy of these facets, subsequently prohibits the enlargement in a , b planes and drives the growth of nuclei along the directions of $[0\ 1\ 0]$ [38].

The relationship between doping ions and metal oxides has been paid more attention in the previous reports [39–42]. In order to understand this point of Er^{3+} doped bismuth molybdate, the

chemical states of 1.0 mol% Er^{3+} doped Bi_2MoO_6 nanosheets were carefully checked by the X-ray photoelectron spectroscopy (XPS) (Fig. 5). The binding energy of $\text{Bi}\ 4f\ 7/2$ is 159.1 eV, which is 0.5 eV higher than that of pure bismuth molybdate (158.6 eV), due to the increase of the electron density around the Bi^{3+} ions when doped with Er^{3+} ions. The binding energy of $\text{Er}\ 4d\ 5/2$ increased to 168.9 eV, whereas the binding energy was reported to be 168.0 eV

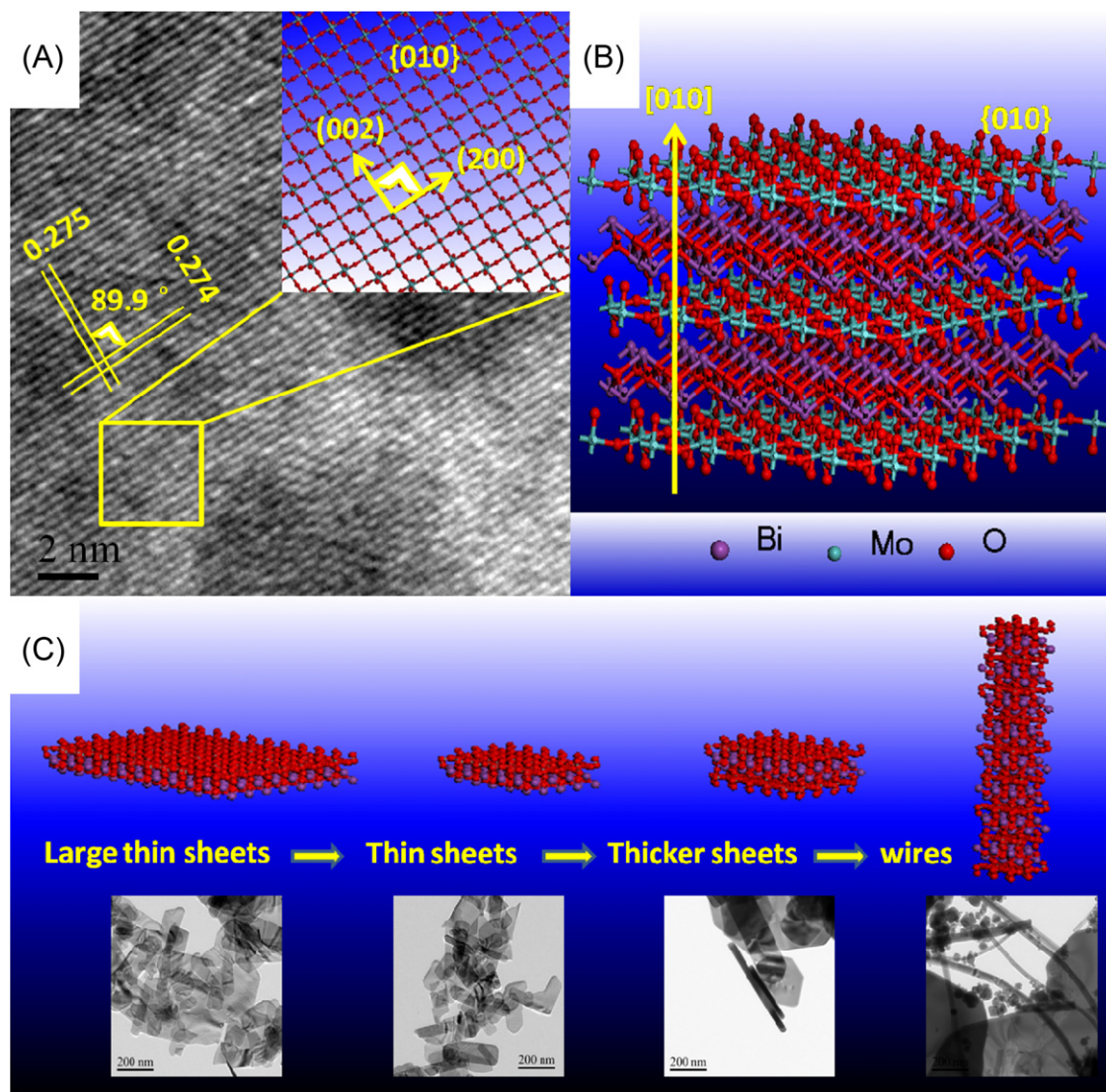


Fig. 4. (A) HRTEM images of 1.0% Er^{3+} doped Bi_2MoO_6 prepared at pH 8, the inset in A is {010} facet, (B) the structure model illustration of Bi_2MoO_6 crystals, and (C) a possible formation process from the large thin sheets to wires.

in erbium oxide [43]. The value of 231.9 eV and 231.8 eV for Mo 3d 5/2 can be assigned to a Mo^{6+} oxidation state and without obvious displacement [44]. As shown in Fig. 5, the peaks of the fitting curves for these four spectra are attributed to the bond of Bi–O at 529.6 eV, the bond of Mo–O at 529.9 eV, the bond of Er–O at 529.1 eV, and the bond of C=O at the surface of Bi_2MoO_6 bond at 531.2 eV, respectively [43,44], and the binding energy of O 1s reduces from 529.82 eV to 529.68 eV due to the Er^{3+} doped into the Bi_2MoO_6 . These results indicate that the Bi–O–Er bonds may have been formed in the Er^{3+} doped Bi_2MoO_6 samples. In addition, the atomic relative abundance of Er^{3+} (at.%, Er: Bi_2MoO_6) was calculated to be about 1.02% according to the XPS analysis, close to the experimental value of 1.0 mol%.

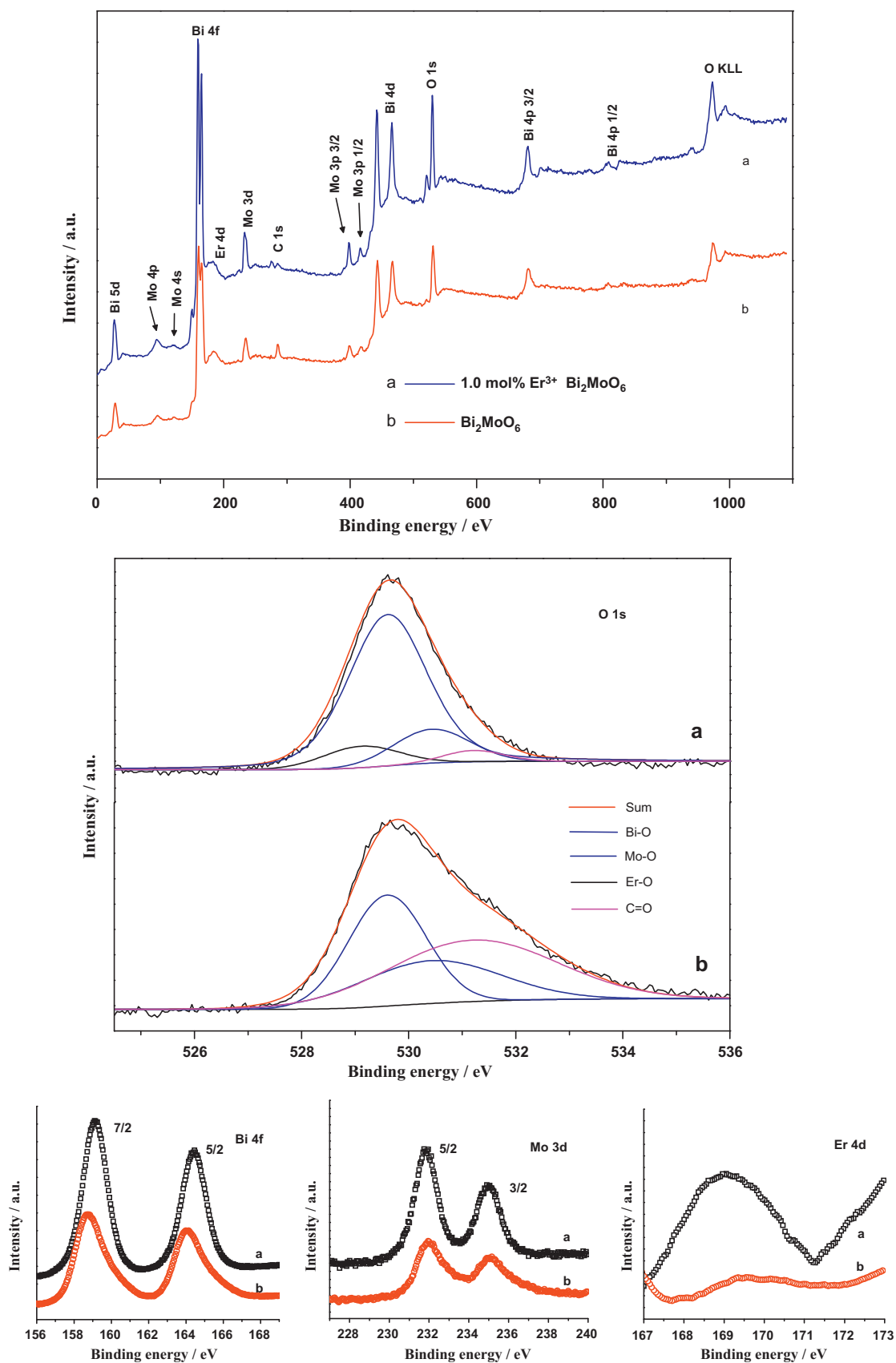
3.2. Optical property

The optical properties of the undoped and Er^{3+} -doped Bi_2MoO_6 were measured using UV–vis diffuse reflection spectrum in the wavelength range of 250–800 nm. Fig. 6 displays UV–visible absorption spectra of the Bi_2MoO_6 samples. All of the Bi_2MoO_6 nanosheets showed absorption of visible light which may produce photoexcited species available for photocatalytic degradation of

dyes and phenol. It was reported from the electronic structure estimated by the plane wave density functional theory that the conduction bands of Bi_2MoO_6 is formed by hybrid of Bi 6s and O 2p orbitals and the Bi 6p and Mo 4d hybrid orbitals are the main contribution to the valence band [45]. For crystalline semiconductors, the optical absorption near the band edge follows the equation:

$$\alpha h\nu = A(h\nu - E_g)^{n/2}$$

in which α , ν , A , and E_g , respectively, the absorption coefficient, light frequency, proportionality constant, and band gap, and n equals 1 or 4, depending on whether the transition is direct or indirect, respectively [46]. The band gap energies of Bi_2MoO_6 nanosheets and Er^{3+} doped Bi_2MoO_6 are calculated to be 2.60 and 2.59 eV, indicating that the Bi_2MoO_6 nanosheets have potential ability for photocatalysis under visible light irradiation and Er^{3+} doping does not change on the crystalline phase of Bi_2MoO_6 . Compared with pure Bi_2MoO_6 , three new absorption bands centered at ca. 487, 523 and 654 nm were observed for Er^{3+} doped Bi_2MoO_6 , which could be assigned to the transitions from the $^4\text{I}_{15/2}$ ground state to $^4\text{F}_{7/2}$, $^2\text{H}_{11/2}$, and $^4\text{F}_{9/2}$ states of Er^{3+} , respectively (Fig. 7) [47]. The effect of Er^{3+} on the recombination of electron–hole of Bi_2MoO_6 was investigated with photoluminescence (PL) spectra. Fig. 8 shows the PL spectra of



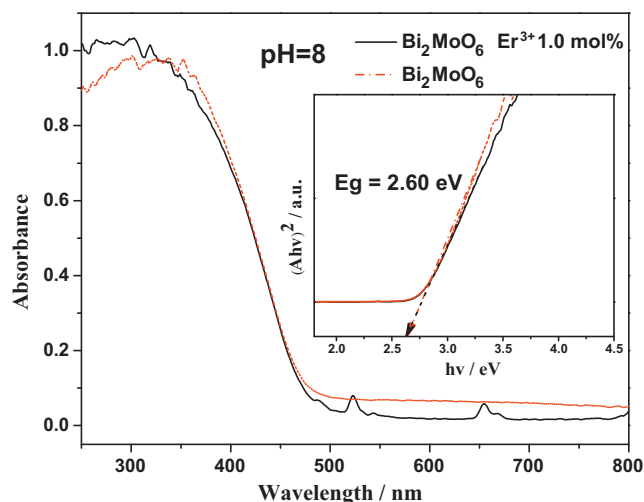


Fig. 6. UV-vis diffuse reflectance spectra of 1.0% Er^{3+} doped Bi_2MoO_6 nanosheets and undoped Bi_2MoO_6 , the inset is band gap evaluation from the plots of $(\alpha h\nu)^2$ vs $h\nu$.

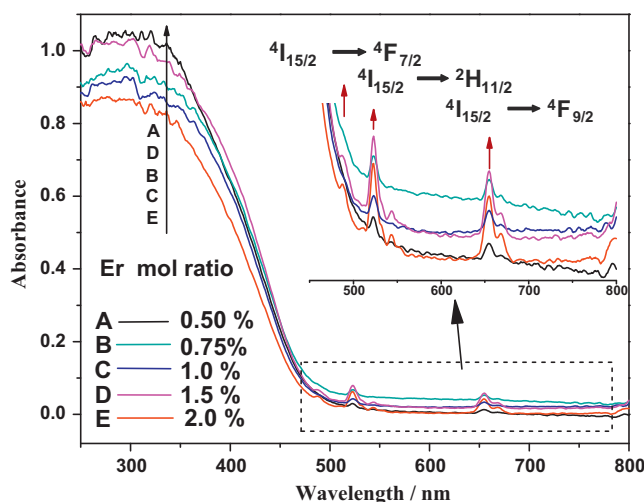


Fig. 7. UV-vis diffuse reflectance spectra of the as-prepared Bi_2MoO_6 nanosheets with different Er^{3+} concentrations.

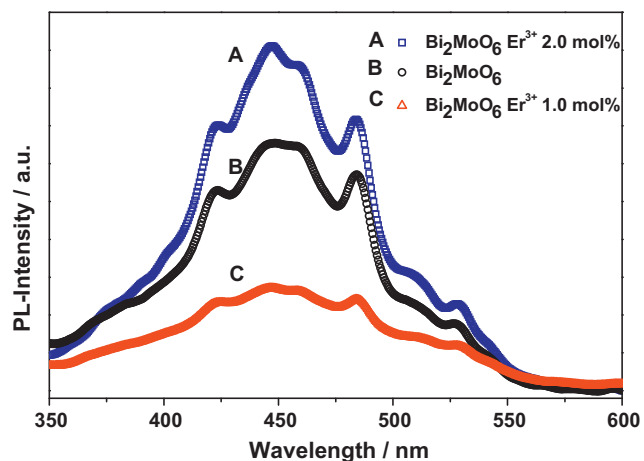


Fig. 8. Photoluminescence spectra of Bi_2MoO_6 and different contents of Er^{3+} doped Bi_2MoO_6 excited by $\lambda_{\text{EX}} = 320$ nm at room temperature.

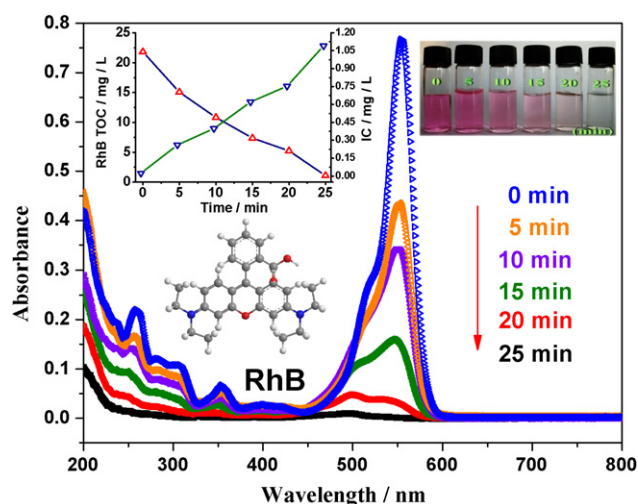


Fig. 9. Time-dependent color change (see the photo in the upper inset), temporal change in total organic carbon (TOC), inorganic carbon (IC) and corresponding time-dependent optical absorbance spectra of the RhB solution (starting concentration: 1.0×10^{-5} M, 50 mL) in the presence of the 1.0 mol% Er^{3+} doped Bi_2MoO_6 nanosheets (50 mg) after its exposure to simulated sunlight for different durations. (For interpretation of the references to color in this figure legend, the reader is referred to the web version of the article.)

pure Bi_2MoO_6 and Er^{3+} doped Bi_2MoO_6 in the range of 350–600 nm excited by 320 nm. There was a significant decrease in the intensity of PL spectra of 1.0 mol% Er^{3+} -doped Bi_2MoO_6 compared to that of pure Bi_2MoO_6 , which implied that the recombination rate of electron–hole pairs is restrained effectively due to the Er^{3+} doped on Bi_2MoO_6 . Moreover, it can be observed that at higher Er^{3+} content, the peak intensities of 2.0 mol% Er^{3+} -doped Bi_2MoO_6 are stronger than that of pure Bi_2MoO_6 . This can be ascribed to extra Er^{3+} behaving as recombinant centers conversely.

3.3. Photocatalytic property

The photocatalytic activity of the Bi_2MoO_6 was investigated by decomposition of rhodamine-B (RhB) and phenol, which are widely used model pollutants for photodecomposition [48–53]. Fig. 9 shows the optical absorption spectra of a RhB aqueous solution (initial concentration: 1.0×10^{-5} M, 50 mL) with 50 mg 1.0 mol% Er^{3+} -doped Bi_2MoO_6 nanosheets after exposure to simulated sunlight for different durations. The main absorption peak at 554 nm corresponding to the RhB molecules, decreases rapidly with extension of the exposure time, and completely disappears after about 25 min. Further exposure leads to no absorption peak in the whole spectrum, which indicates the complete decomposition of RhB. A series of color changes of the sample is shown in the inset of Fig. 9, which corresponds to the sequential changes of the absorption measurements. It is clear that the intense bright cherry-red color of the starting solution gradually disappears with increasing exposure time under the simulated sunlight. In order to further investigate the photodegradation of RhB, Fig. 9 illustrates the total organic carbon (TOC) removal and inorganic carbon (IC) during the mineralization of RhB by Er^{3+} -doped Bi_2MoO_6 under simulated sunlight irradiation. TOC removal efficiency increases to 94.6% after 30 min, accompanying a steady increase of the concentration of IC in the solution as shown in Fig. 9. These results indicated that RhB solution can not only be discolored but also be mineralized efficiently in the Er^{3+} -doped Bi_2MoO_6 /RhB system.

The photocatalytic activity depends on the morphology and Er^{3+} content. As shown in Fig. 10A, the photocatalytic activities for decomposition of RhB of Bi_2MoO_6 have a maximum value with the increase of pH value. The Bi_2MoO_6 nanosheets prepared at pH 8

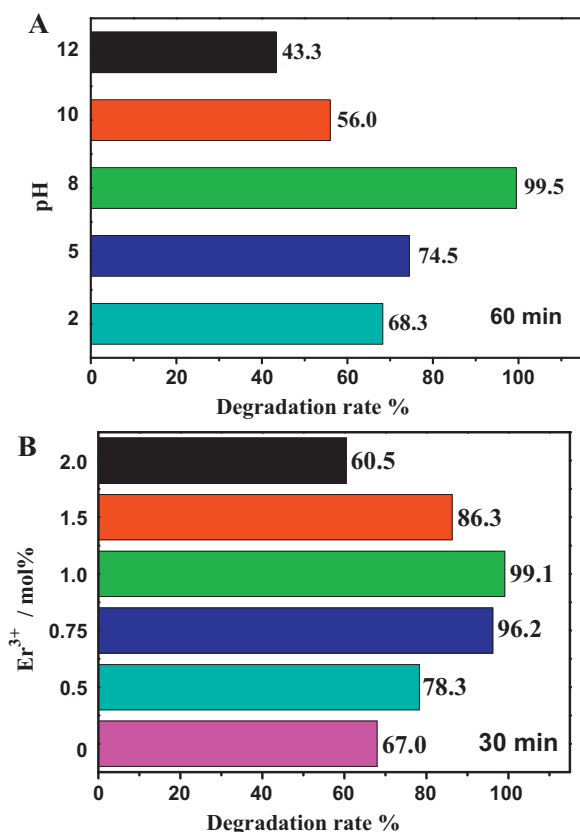


Fig. 10. Photodecomposition of aqueous RhB solution under simulated sunlight, (A) Bi₂MoO₆ samples with different pH values and (B) Bi₂MoO₆ nanosheets prepared at pH 8 with different Er³⁺ concentrations.

exhibited the highest photocatalytic activity among these catalysts synthesized in different pH values, RhB dye could be completely degraded in 60 min under simulated sunlight irradiation. But, only 43.3% of RhB was degraded over Bi₂MoO₆ nanowires which were prepared under the alkaline condition (pH 12). The shape and crystal orientation of the Bi₂MoO₆ nanoparticles are characterized by transmission electron microscopy (TEM) and X-ray diffraction (XRD), which reveals that the nanosheets selectively expose {010} facets as the main external surfaces and the nanowires grow along the (010) direction. It is well known that photocatalysts with higher surface areas can absorb more RhB molecules and tend to perform admirable photocatalytic activity. However, in our work Bi₂MoO₆ nanosheets prepared at pH 8 exhibited the highest photocatalytic but not the sample with the highest surface area (see Table 1), and the Bi₂MoO₆ prepared under 8, 10, 12 samples with close surface area values show distinctly different photocatalytic activity. So we believe that the exposed {010} facets may contribute a lot to the enhanced photocatalytic activity.

After optimization of the morphologies of Bi₂MoO₆ by adjusting the pH values, photocatalytic degradation experiment was carried out over Er³⁺ doped Bi₂MoO₆ under the same conditions. To differentiate the decomposed rate of Bi₂MoO₆ nanosheets doped with different Er³⁺ contents, the experiments were carried out under the simulated sunlight. These results are shown in Fig. 10B. From the above results, the best photocatalytic performance was

Table 1
BET surface areas of the samples prepared under different pH values.

Sample	pH 2	pH 5	pH 8	pH 10	pH 12
BET surface areas (m ² g ⁻¹)	3.91	9.40	4.49	4.03	3.79

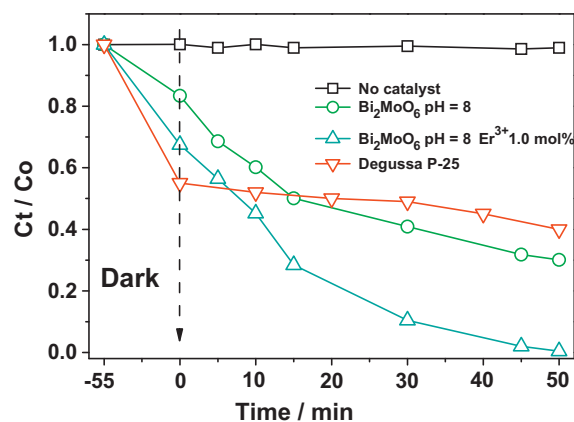


Fig. 11. Photodecomposition activity of decomposition of aqueous RhB solution without and with catalysts under visible light.

observed when the Er³⁺ concentration was 1.0 mol%. The photocatalytic activities of the Er³⁺ doped Bi₂MoO₆ catalysts increased gradually as the Er³⁺ concentration increased until the Er³⁺ concentration reached 1.0 mol%. When the Er³⁺ concentration was more than 1.0 mol%, the photocatalytic activity decreased sharply, which were even lower than that of the undoped Bi₂MoO₆. This can be explained as follows: there are two possible upconversion processes in the Er³⁺ doped hosts, excited state absorption (ESA) process is a single ion process and is independent of the Er³⁺ ions concentration, while energy transfer (ET) process involves two ions. ET between Er³⁺ ions can be neglected with a concentration of 1.0 mol% or lower due to the random distribution of dopant ions in the host lattice at relatively low concentration [54]. However, at higher concentration, the distances between two Er³⁺ ions are shortened, thus leading to the formation of Er³⁺ clusters and the ET becomes the dominant process, which may lead to self-quenching that is detrimental for the whole upconversion efficiency [55]. In our Er³⁺ doped Bi₂MoO₆ system, when the Er³⁺ concentration reached 1.5 mol%, the formed Er³⁺ clusters not only led to serious non-radiative concentration quenching, but also acted as electron-hole recombination centers, resulting in low photocatalytic activity.

To demonstrate the relationship between the morphology, Er³⁺ content and enhancement of the photocatalytic performance of the nanostructured Bi₂MoO₆, a further experiment was performed using Er³⁺ doped Bi₂MoO₆ nanosheets, undoped Bi₂MoO₆ and Degussa P25. Without any catalyst, only a slight decomposition (less than 1%) of RhB was detected under visible light irradiation for 50 min (Fig. 11). The addition of catalysts leads to obvious degradation of RhB. After the organics adsorption/desorption over the catalyst for 55 min and 50 min visible light irradiation, about 52% of RhB was decomposed over Degussa P25, which is lower than Er³⁺ doped Bi₂MoO₆ nanosheets and undoped Bi₂MoO₆. More than 99% of RhB was degraded over Er³⁺ doped Bi₂MoO₆ nanosheets. Both of the Er³⁺ doping Bi₂MoO₆ nanosheets and undoped Bi₂MoO₆ are much superior to that of Degussa P25, indicating the advantage of the exposed {010} facets as the main external surfaces and using Er³⁺ as an UC reagent which could transform visible light into ultraviolet light. In addition to RhB, phenol, a typical colorless contaminant was chosen as a goal pollutant which has no light absorption characteristics in the visible light region. Fig. 12 shows that 1.0 mol% Er³⁺ doped Bi₂MoO₆ nanosheets exhibited much higher photodegradation efficiency than Degussa P25, they could degrade 78.3 and 46.4% of phenol in 120 min, respectively. Many new peaks appeared in the case of Degussa P25 TiO₂ photocatalysis, because it has proposed that phenol is first oxidized to hydroquinone, p-benzoquinone or muconaldehyde and then these

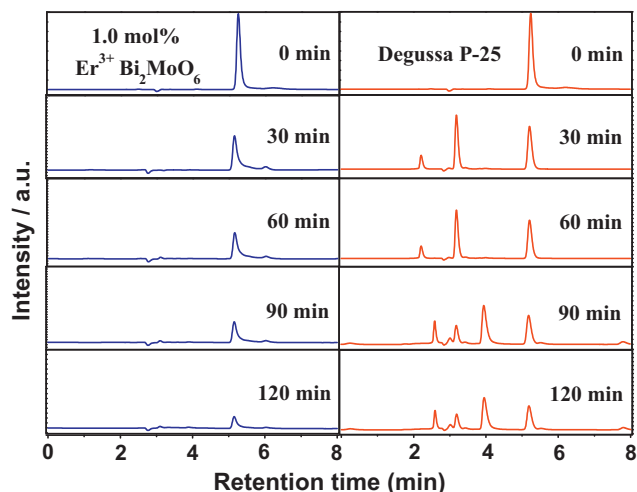


Fig. 12. High performance liquid chromatography (HPLC) analysis of phenol photodegradation over Er^{3+} doped Bi_2MoO_6 nanosheets and Degussa P25 under simulated sunlight irradiation.

products are converted into CO_2 via many oxidation steps [56]. Unlike the Degussa P25, all peaks decrease with extension of the exposure time that may attribute to the strong oxidation activity of Er^{3+} doped Bi_2MoO_6 nanosheets. The mineralization degree of phenol was examined by measuring the decrease in TOC of the reaction solution. TOC variation during the photodegradation of phenol in the system under simulated sunlight irradiation is depicted in Fig. 13. As shown in Fig. 13, the TOC decreased gradually. After irradiation for 120 min, 74.8% TOC is removed. However, in the phenol/ TiO_2 (P25) system, only 49.4% phenol is mineralized within 120 min.

The photocatalysis mechanism of Er^{3+} doped Bi_2MoO_6 nanosheets can be explained as follows: as it is shown in Fig. 14, the upconversion reagent Er^{3+} can be easily excited by solar light as excitation source [57]. Thus, the upconversion process may easily take place in Er^{3+} doped Bi_2MoO_6 , and the upconversion process conforms to the energy level data shown in the images. The upconversion mechanism is based on ground state absorption (GSA) and excited state absorption (ESA). When the Er^{3+} is pumped by 652.2–657.8 nm photons in solar light, the upconversion signals at 318.7 and 320.1 nm are also found by 487 and 523 (or 548.8) nm light excitation, which is in accordance with the UV–vis diffuse

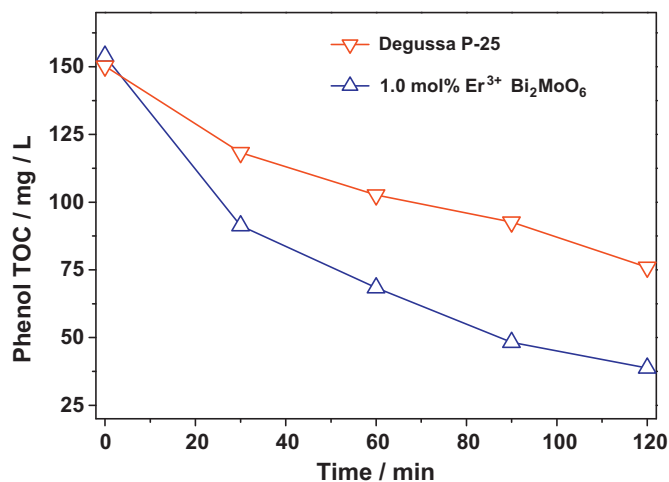


Fig. 13. Total organic carbon (TOC) analysis of phenol photodegradation over Er^{3+} doped Bi_2MoO_6 nanosheets and Degussa P25 under simulated sunlight irradiation.

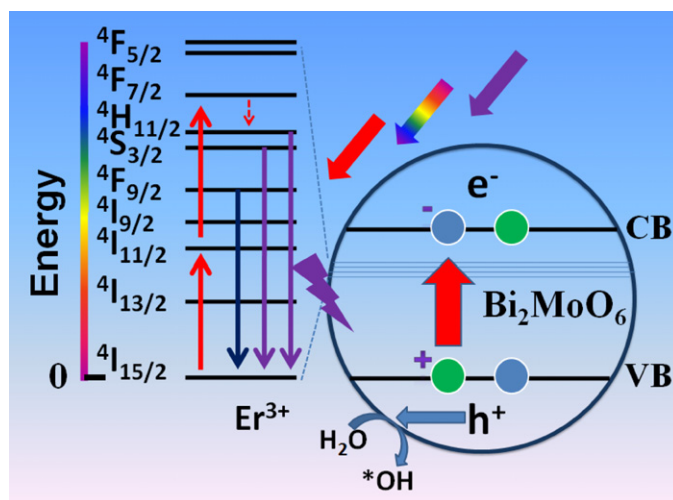


Fig. 14. Schematic illustration of the energy conversion and the photocatalytic process using an upconverter.

reflection results. After capturing the NIR and visible light photons in solar light, Er^{3+} emits relatively strong visible and ultraviolet which matches very well with the band-gap of Bi_2MoO_6 . Thus the electron and hole pairs are yielded at the same time. Then the highly oxidative holes accumulated in the Bi_2MoO_6 can directly decompose the organic pollutants or react with H_2O molecules to produce $\cdot\text{OH}$.

4. Conclusions

Bi_2MoO_6 nanosheets were synthesized by a hydrothermal method. The morphology of Bi_2MoO_6 can be controlled by adjusting the pH values, Er^{3+} doped Bi_2MoO_6 nanosheets is found to be highly effective for photocatalytic degradation of dyes and phenol, which is much superior to that of Degussa P25. The exposed main external surfaces are {0 1 0} facets. The high photodecomposition activity can be attributed to the exposed {0 1 0} facets and the doped Er^{3+} . The introduction of the upconverter Er^{3+} in photocatalyst will provide new strategies to enhance the efficiency of photocatalysts.

Acknowledgements

This work is supported by National Natural Science Foundation of China (20803096, 21073238), the NSF of Hubei Province (Distinguished Young Investigator Grant 2010CDA082), the Scientific Research Foundation for the Returned Overseas Chinese Scholars, State Education Ministry, and National Basic Research Program of China (Grant No: 2011CB211704).

References

- [1] X. Chen, S. Shen, L. Guo, S.S. Mao, Chem. Rev. 110 (11) (2010) 6503–6570.
- [2] G. Palmisano, V. Augugliaro, M. Pagliaro, L. Palmisano, Chem. Commun. (2007) 3425–3437.
- [3] A. Kudo, Y. Miseki, Chem. Soc. Rev. 38 (2009) 253–278.
- [4] J. Sato, T. Nishikawa, S. Miyagishi, Appl. Catal. B: Environ. 79 (2008) 117–121.
- [5] Y. Liu, L. Chen, J. Hu, J. Li, R. Richards, J. Phys. Chem. C 114 (2010) 1641–1645.
- [6] Y. Liu, J. Hu, J. Li, J. Alloys Compd. 509 (2011) 5152–5158.
- [7] X. Chen, L. Liu, P.Y. Yu, S.S. Mao, Science 331 (2011) 746–750.
- [8] Y. Xu, Y. Zhuang, X. Fu, J. Phys. Chem. C 114 (2010) 2669–2676.
- [9] M. Wu, Y. Jin, G. Zhao, M. Li, D. Li, Environ. Sci. Technol. 44 (2010) 1780–1785.
- [10] K. Lv, Q. Xiang, J. Yu, Appl. Catal. B: Environ. 104 (2010) 275–281.
- [11] G.P. Mane, A. Vinu, S.D. Naik, D.P. Amalnerkar, B.B. Kale, Small 7 (2011) 957–964.
- [12] J. Su, X. Feng, J.D. Sloppy, L. Guo, C.A. Grimes, Nano Lett. 11 (1) (2011) 203–208.
- [13] G. Xi, J. Ye, Chem. Commun. 46 (2010) 1893–1895.
- [14] F. Amano, A. Yamakata, K. Nogami, M. Osawa, B. Ohtani, J. Am. Chem. Soc. 130 (2008) 17650–17651.
- [15] G. Li, D. Zhang, J.C. Yu, K.H. Michael, Environ. Sci. Technol. 44 (11) (2010) 4276–4281.

- [16] T. Zhou, J. Hu, *Environ. Sci. Technol.* 44 (2010) 8698–8703.
- [17] E.L. Cates, M. Cho, J. Kim, *Environ. Sci. Technol.* 45 (8) (2011) 3680–3686.
- [18] J. Wang, P.A. Tanner, *J. Am. Chem. Soc.* 132 (2010) 947–949.
- [19] G. Wang, Q. Peng, Y. Li, *J. Am. Chem. Soc.* 131 (2009) 14200–14201.
- [20] F. Wang, J. Wang, X. Liu, *Angew. Chem. Int. Ed.* 49 (2010) 7456–7460.
- [21] S. Heer, K. Kömpe, H.U. Güdel, M. Haase, *Adv. Mater.* 16 (2004) 2102–2105.
- [22] C.J. Johnson, E. Dujardin, S.A. Davis, C.J. Murphy, S. Mann, *J. Mater. Chem.* 12 (2002) 1765–1770.
- [23] V. Marinova, M. Veleva, *Opt. Mater.* 19 (2002) 329–333.
- [24] J. Jung, H. Kim, A. Choi, Y. Chung, T. Kim, S. Lee, S. Ohb, I.K. Song, *Catal. Commun.* 8 (2007) 625–628.
- [25] X. Zhao, J. Qu, H. Liu, C. Hu, *Environ. Sci. Technol.* 41 (2007) 6802–6807.
- [26] G. Tian, Y. Chen, W. Zhou, K. Pan, Y. Dong, C. Tian, H. Fu, *J. Mater. Chem.* 21 (2011) 887–892.
- [27] A. Kudo, *Int. J. Hydrogen Energy* 32 (2007) 2673–2678.
- [28] G. Shan, G.P. Demopoulos, *Adv. Mater.* 22 (2010) 4373–4377.
- [29] V. Badescu, A.M. Badescu, *Renew. Energy* 34 (2009) 1538–1544.
- [30] J. Wang, R. Li, Z. Zhang, W. Sun, R. Xu, Y. Xie, Z. Xing, X. Zhang, *Appl. Catal. A: Gen.* 334 (2008) 227–233.
- [31] C. Li, F. Wang, J. Zhu, J.C. Yu, *Appl. Catal. B: Environ.* 100 (2010) 433–439.
- [32] Z. Zhang, W. Wang, W. Yin, M. Shang, L. Wang, S. Sun, *Appl. Catal. B: Environ.* 101 (2010) 68–73.
- [33] S.H. Yu, L. Biao, M.S. Mo, J.H. Huang, X.M. Liu, Y.T. Qian, *Adv. Funct. Mater.* 13 (2003) 639–647.
- [34] Y.W. Jun, J.S. Choi, J. Cheon, *Angew. Chem. Int. Ed.* 45 (2006) 3414–3439.
- [35] N. Kim, R.N. Vannier, C.P. Grey, *Chem. Mater.* 17 (2005) 1952–1958.
- [36] L. Zhang, T. Xu, X. Zhao, Y. Zhu, *Appl. Catal. B: Environ.* 98 (2010) 138–146.
- [37] H.W. Liao, Y.F. Wang, X.M. Liu, Y.D. Li, Y.T. Qian, *Chem. Mater.* 12 (2000) 2819–2821.
- [38] H.L. Wang, X.D. Ma, X.F. Qian, J. Yin, Z.K. Zhu, *J. Solid State Chem.* 177 (2004) 4588–4596.
- [39] T. Liu, P. Lao, I. Lo, *Sci. Total Environ.* 407 (2009) 3407–3414.
- [40] J. Zhong, F. Chen, J.L. Zhang, *J. Phys. Chem. C* 114 (2010) 933–939.
- [41] W. Ren, Z. Ai, F. Jia, L. Zhang, X. Fan, Z. Zou, *Appl. Catal. B: Environ.* 69 (2007) 138–144.
- [42] K. Lv, H. Zuo, J. Sun, K. Deng, S. Liu, X. Li, D. Wang, *J. Hazard. Mater.* 161 (2009) 396–401.
- [43] B.F. Dzhurinskii, D. Gati, N.P. Sergushin, V.I. Nefedov, Y.V. Salyn, *Russ. J. Inorg. Chem.* 20 (1975) 2307–2314.
- [44] D. Briggs, M.P. Seah, *Practical Surface Analysis*, vol. 1, second ed., John Wiley & Sons, 1993.
- [45] M. Long, W. Cai, H. Kisch, *Phys. Lett.* 461 (2008) 102–105.
- [46] M.A. Butler, *J. Appl. Phys.* 48 (1977) 1914.
- [47] D.K. Chatterjee, M.K. Gnanasammandhan, Y. Zhang, *Small* 6 (2010) 2781–2795.
- [48] M. Shang, W. Wang, J. Ren, S. Sun, L. Zhang, *Nanoscale* 3 (2011) 1474–1476.
- [49] Y. Lu, T. Lunkenbein, J. Preussner, S. Proch, J. Breu, R. Kempe, M. Ballauff, *Langmuir* 26 (2010) 4176–4183.
- [50] J.H. Huang, Y.J. Cui, X.C. Wang, *Environ. Sci. Technol.* 44 (2010) 3500–3504.
- [51] H. Yu, B. Tian, J. Zhang, *Chem. Eur. J.* 17 (2010) 5499–5502.
- [52] X. Hu, G. Li, J.C. Yu, *Langmuir* 26 (5) (2010) 3031–3039.
- [53] L. Zhang, K. Wong, Z. Chen, J.C. Yu, J. Zhao, C. Hu, C. Chang, P. Wong, *Appl. Catal. A* 363 (2009) 221–229.
- [54] F. Wang, Y. Han, C. Lim, Y. Lu, J. Wang, J. Xu, H. Chen, C. Zhang, M. Hong, X. Liu, *Nature* 463 (2010) 1061–1065.
- [55] S. Ivanova, F. Pellé, *J. Opt. Soc. Am. B* 26 (2009) 1930–1938.
- [56] H. Park, W. Choi, *Catal. Today* 101 (2005) 291–297.
- [57] R. Xu, J. Li, J. Wang, X. Wang, B. Liu, B. Wang, X. Luan, X. Zhang, *Sol. Energy Mater. Sol. Cells* 94 (2010) 1157–1165.